Modified Ångström exponent for the characterization of submicrometer aerosols

Norm T. O'Neill, Oleg Dubovik, and Tom F. Eck

The classical Ångström exponent is an operationally robust optical parameter that contains size information on all optically active aerosols in the field of view of a sunphotometer. Assuming that the optical effects of a typical (radius) size distribution can be approximated by separate submicrometer and supermicrometer components, we show that one can exploit the spectral curvature information in the measured optical depth to permit a direct estimation of a fine-mode (submicrometer) Ångström exponent (α_f) as well as the optical fraction of fine-mode particles (η). Simple expressions that enable the estimation of these parameters are presented and tested by use of simulations and measurements. © 2001 Optical Society of America

OCIS codes: 010.1290, 280.1100.

1. Introduction

Users of sunphotometry data understand and exploit the fact that the Ångström exponent[1] contains a mixture of information on intensive aerosol properties (size and refractive index) and extensive aerosol properties (vertically integrated number density or abundance) from both the fine (submicrometer radius) and course (supermicrometer radius) modes of the size distribution. Given the simplicity and robustness of this parameter it is of some relevance to ascertain whether a purely fine-mode analog of the Ångström exponent can be extracted directly from measured optical depth spectra. If one recognizes that much of the spectral behavior of the total Ångström exponent is induced by extensive particle number variations of the two fundamental modes,[2] then it is reasonable to expect that spectral curvature analysis will yield intensive information on the fine-mode Ångström exponent.

This type of approach is useful when one wants to compare large or disparate data sets of spectral optical depth for bulk fine particle size distribution information without going through detailed particle size distribution inversions. It also has the advantage of eliminating the dependence of the size distribution parameterization on intermediate parameters of the inversion (such as smoothing constraints or choice and nature of the inversion parameters) and, in general, of reducing the complexity of the processing chain and the reproducibility of data archives for information that is fundamentally optical in nature. An example of a practical application would be the systematic comparison of fine-mode size information for small to intermediate optical depths; whereas at large optical depths the accumulation mode is typically dominant for smoke or urban aerosols,[3,4] one cannot be sure for small to intermediate optical depths just what fraction of the variation in the Ångström exponent is due to particle number influence and what fraction is due to actual changes in the average size of the accumulation mode.

A fine-mode Ångström exponent itself is a useful indicator of particle type (size and refractive index), but also is strongly related to measures of average fine-mode particle radius.[5,6] The extraction of this exponent thus leads directly to robust estimates of average fine-mode particle size that often represent the extent of actual size information required by users of optical data. In this paper we focus on the methodology for the extraction of the fine-mode Ång-

When this research was performed, all the authors were with the NASA Goddard Space Flight Center, Greenbelt, Maryland 20771. N. T. O'Neill was on leave from the Centre d'Applications et de Recherches en Teledetection, Université de Sherbrooke, 2500 Boulevard Université, Sherbrooke, Québec J1K 2R1, Canada. O. Dubovik is also with Science Systems and Applications, Inc., 5900 Princess Garden Parkway, Suite 300, Lanham, Maryland 20706. T. F. Eck is also with the Goddard Earth Sciences and Technology Center, University of Maryland Baltimore County, 1000 Hilltop Circle, Baltimore, Maryland 21250.

ström exponent rather than the physical interpretation of a derived average particle size.

So that the mathematical foundation for the estimation of the fine-mode Ångström exponent be rigorous, it is necessary to work with a monochromatic Ångström exponent rather than the classical multi-wavelength Ångström exponent. The latter is defined, for a given spectral range of aerosol optical depth data, by a linear regression of optical depth versus wavelength (linear in log–log space).[1] The mathematical development for monochromatic Ångström exponents was dealt with in a previous paper in which we employed a third-order spectral polynomial regression over the visible and near-infrared spectral range to permit the computation of first- and second-order spectral derivatives at any wavelength.[2] The monochromatic Ångström exponent at a particular wavelength λ can be defined rigorously as

$$\alpha(\lambda) = -\frac{d \ln \tau_a(\lambda)}{d \ln \lambda}, \qquad (1)$$

where $\tau_a(\lambda)$ is the total aerosol optical depth. Given that $\tau_a(\lambda)$ is the sum of fine- and coarse-mode optical depths, this expression can in turn be written as a weighted function of fine- and coarse-mode terms[2,5,6]:

$$\alpha(\lambda) = \frac{\alpha_f(\lambda)\tau_f(\lambda) + \alpha_c(\lambda)\tau_c(\lambda)}{\tau_a(\lambda)}$$
$$= \alpha_f(\lambda)\eta(\lambda) + \alpha_c(\lambda)[1 - \eta(\lambda)], \qquad (2)$$

where $\alpha_f(\lambda)$ and $\tau_f(\lambda)$ are the fine-mode Ångström exponent and optical depth, $\alpha_c(\lambda)$ and $\tau_c(\lambda)$ are the coarse-mode Ångström exponent and optical depth, and $\eta(\lambda) = \tau_f(\lambda)/\tau_a(\lambda)$. If the local atmosphere goes through an influx or outflux of particles of the same type (abundance or particle number change), then only $\eta(\lambda)$ varies.

Differentiating Eq. (2) yields the spectral derivative[2]

$$\alpha'(\lambda) = \alpha_f'(\lambda)\eta(\lambda) + \alpha_c'(\lambda)[1 - \eta(\lambda)]$$
$$- \eta(\lambda)[1 - \eta(\lambda)][\alpha_f(\lambda) - \alpha_c(\lambda)]^2. \qquad (3)$$

We emphasize that these are exact differential equations at a particular wavelength and that there is no need or indeed desire to assume spectral constancy in the Ångström exponents. Rather they are to be viewed as instantaneous derivatives at a particular wavelength and interpreted in terms of their tangential equivalence to the classical Ångström exponent and its associated Junge-type size distribution.[7]

Our purpose in this paper is to demonstrate that monochromatic values of $\alpha_f(\lambda)$ can be extracted directly from measurements of the first- and second-order spectral derivatives of aerosol optical depth [$\alpha(\lambda)$ and $\alpha'(\lambda)$]. Furthermore, a by-product of the extraction algorithm is that the optical fraction of fine-mode particles in the atmospheric column [$\eta(\lambda)$] can be estimated.

When we use a vector space analogy (and drop the explicit wavelength dependence), the operation of ex-

tracting a fine-mode Ångström exponent is not unlike an axis rotation to extract one of the basis vectors (α_f and α_c) where these basis vectors generate the (vector space of) Ångström exponents (α). The members of this vector space are generated when fractional optical depth multipliers [η and $(1 - \eta)$] are applied to the basis vectors. These multipliers, in the case of fixed particle types, are largely dependent on the extensive property of abundance or particle number.

2. Simple Expressions for the Estimation of α_f and η

By combining Eqs. (2) and (3) one arrives at a simple symmetric relationship between the measured (total) spectral derivatives and the constituent (modal) spectral derivatives at a given wavelength λ:

$$t = (\alpha - \alpha_c) - \frac{(\alpha' - \alpha_c')}{(\alpha - \alpha_c)} = (\alpha_f - \alpha_c) - \frac{(\alpha_f' - \alpha_c')}{(\alpha_f - \alpha_c)}, \qquad (4)$$

where t can be viewed as a transformation of measured parameters (α and α'), which is invariant in the presence of abundance-induced changes in these parameters (i.e., in the presence of changes in τ_f or τ_c caused by particle number variations of either component). Solving for the term in α_f yields the quadratic:

$$(\alpha_f - \alpha_c) = \frac{1}{2}\{t + [t^2 + 4(\alpha_f' - \alpha_c')]^{1/2}\} \qquad (5)$$

where the plus sign in front of the radical is required to ensure that the right side reduces to α_f if the coarse-mode optical depth tends toward zero. Having solved for ($\alpha_f - \alpha_c$), we can then evaluate the optical ratio η using Eq. (2):

$$\eta = \frac{(\alpha - \alpha_c)}{(\alpha_f - \alpha_c)}. \qquad (6)$$

A common feature of the coarse-mode optical depth is the lack of variation across the visible spectral region. This can be exploited to solve for α_f in terms of measurable quantities if we assume that the coarse-mode Ångström exponent and its spectral derivative are zero or close to zero. In fact the values employed in our algorithm ($\lambda = 500$-nm wavelength) were $\alpha_c = -0.15$ and $\alpha_c' = 0.0$. These values are close to the measured mean for the ensemble of coarse-mode distributions presented in Subsection 4.C. Independent Mie calculations for a sampling of model coarse-mode distributions yielded values of α_c that varied from -0.02 to -0.12 and values of α_c' between -0.04 and -0.08 (Table 1). Although the algorithmic value of α_c was slightly less than these modeled results, we simply ascribe the difference to an uncertainty of approximately $\Delta\alpha_c = 0.15$.

The term involving α_f' is of course not known, but it can be constrained; a sampling of log-normal size distributions[11] for σ_g between 0.4 and 0.6 [or $\exp(\sigma_g)$ between 1.5 and 1.8]; geometric mean radius r_g between 0.05 and 0.4; and refractive indices of 1.5–

Mode	r_N (μm)	σ	r_{eff} (μm)	Refractive Index	α_c	$\alpha_c{'}$
WCP[a]	0.5	2.5	4.08	1.5–0i	−0.085	−0.042
Soil[b]	0.43	2.2	2.04	1.525–0.005i	−0.12	−0.086
Fog[c]					−0.02 to−0.06	N/A[d]

[a]Close to dustlike parameters.[8]
[b]Case of low dust loading.[9]
[c]Range for advection and radiance fogs in Ref. 10.
[d]N/A, not applicable.

0.0035i, 1.43–0.0035i, and 1.33–0i yielded the following approximate relationship at λ = 500 nm:

$$\alpha_f{'} = a\alpha_f^2 + b\alpha_f + c, \qquad (7)$$

where $a = -0.22$, $b = 0.43$, and $c = 1.4$ and where $|\Delta\alpha_f{'}| < 0.5$ for the points through which this relationship was fitted [note, however, that with an R^2 of approximately 0.14 the parabola of Eq. (7) was only marginally better than if we simply assumed a constant value of approximately 1.6]. The range of input size distribution parameters used to generate Eq. (7) was chosen to represent the type of fine particle sizes found in mid-Atlantic eastern U.S. continental conditions[12] as well as to represent typical refractive indices for conditions ranging from dry to humid.

The range of applicability of Eq. (7) is defined more universally in terms of a variant of van de Hulst's phase-shift parameter ρ (Ref. 13):

$$1 \leq \rho \leq 5, \qquad (8)$$

where

$$\rho = 2kr_{eff}|m - 1| \cong 2(2\pi r_{eff}/\lambda)(m_r - 1),$$

the refractive index $m = m_r - m_i i$, and where the computations were performed for $\lambda = 0.5$ μm. The parameter r_{eff} [$= r_g \exp(2.5 \ln^2 \sigma)$ for a log-normal distribution] is the best estimate of an effective optical radius in the absence of any *a priori* optical information.[11] For $m_r = 1.43$ this constraint translates into $0.09 < r_{eff} < 0.46$ μm. The upper and lower limits of Eq. (8) correspond to the neighborhood of the classical extinction efficiency peak where $\alpha_f \rightarrow 0$ and to the transition regime where absorption effects begin to dominate scattering effects ($\alpha_f \rightarrow 1$).

Applying Eq. (7) to Eq. (5) yields

$$\alpha_f = \frac{1}{2(1-a)} \{(t + b^*) + [(t + b^*)^2$$
$$+ 4c^*(1-a)]^{1/2}\} + \alpha_c, \qquad (9)$$

where $b^* = b + 2\alpha_c$ and $c^* = c - \alpha_c{'} + (b + a\alpha_c)\alpha_c$.

The phase-shift parameter constraint of Eq. (8) when applied to biomass-burning aerosols yielded an $\alpha_f{'}$ versus α_f dependency that could be modeled adequately by the same parameterization as above except that the constant of Eq. (7) is $c = 1.1$ rather than 1.4 ($R^2 = 0.25$ for the residual fit). In this case the aerosols were modeled as concentric shells with a soot core of a refractive index of 1.8–0.6i enclosed in a

shell of a refractive index of 1.5–0i.[3] Log-normal distributions, with the same range of σ_g and r_g values as defined above, were used again. The volume fraction of the soot core was allowed to vary between 6 and 12%.

Figure 1 shows α_f versus α for a set of fixed contour curves in η and α' at the nominal wavelength of 500 nm. Our interpretation of Fig. 1 is that it represents the value of α_f that is required to achieve given values of α and α' for which the variability in α and α' is controlled by a ratio of optical depths (i.e., by η). The separate curves in Fig. 1, which were plotted with either Eq. (2) for the solid (η = constant) coordinates or Eq. (9) for the dashed (α' = constant) coordinates, are purely algebraic in nature and do not account for any physical constraints such that η must be less than unity and that α_f cannot be more than approximately 2.5. Instrumental errors and departures of actual atmospheric conditions from any modeling hypotheses embedded in Eqs. (1)–(9) can of course induce retrieved values of α_f or η that are physically inconsistent. The behavior about the η = 1 line underscores the fundamental algorithmic mechanism of Eq. (5); when we set aside the small contribution of the coarse-mode Ångström parameters, this line represents a pivotal condition where α' = $\alpha_f{'}$ and $\alpha = \alpha_f$. The physically valid region above η = 1 in Fig. 1 is characterized by $\eta < 1$, $\alpha' < \alpha_f{'}$, and $\alpha < \alpha_f$ [these inequalities are better understood when one refers to Eqs. (2) and (5)].

Figure 2 illustrates total (absolute and relative) error magnitude simulations derived from Eq. (9) for
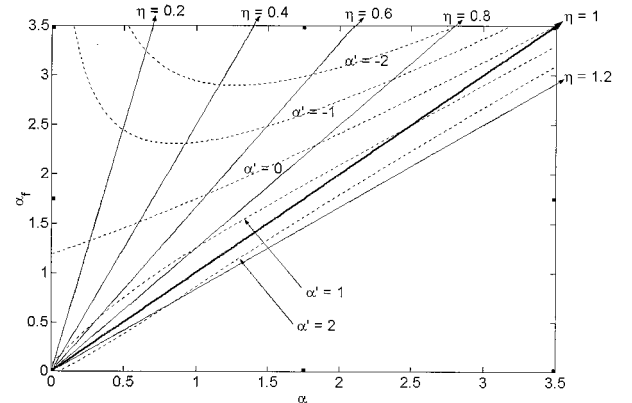

Fig. 1. Algorithmic behavior of Eq. (9) at a wavelength of 500 nm. Constant curves of α' and η are superimposed.
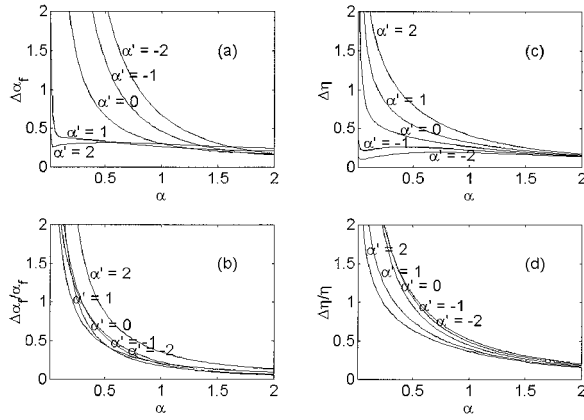
Fig. 2. Simulated total errors in (a) $\Delta\alpha_f$, (b) $\Delta\alpha_f/\alpha_f$, (c) $\Delta\eta$, and (d) $\Delta\eta/\eta$ for the range of conditions illustrated in Fig. 1 and assumed errors in $\Delta\alpha$, $\Delta\alpha'$, $\Delta\alpha_f'$, $\Delta\alpha_c$, and $\Delta\alpha_c'$ (see text for details).

the range of parameterizations illustrated in Fig. 1. We computed the total errors assuming partially incoherent, component errors, namely,

$$\Delta\alpha_f{}^2 = \left(\frac{\partial\alpha_f}{\partial\alpha'}\Delta\alpha' + \frac{\partial\alpha_f}{\partial\alpha}\Delta\alpha\right)^2 + \left(\frac{\partial\alpha_f}{\partial\alpha_f'}\Delta\alpha_f'\right)^2$$
$$+ \left(\frac{\partial\alpha_f}{\partial\alpha_c'}\Delta\alpha_c'\right)^2 + \left(\frac{\partial\alpha_f}{\partial\alpha_c}\Delta\alpha_c\right)^2, \qquad (10)$$

$$\Delta\eta^2 = \left(\frac{\partial\eta}{\partial\alpha'}\Delta\alpha' + \frac{\partial\eta}{\partial\alpha}\Delta\alpha\right)^2 + \left(\frac{\partial\eta}{\partial\alpha_f'}\Delta\alpha_f'\right)^2$$
$$+ \left(\frac{\partial\eta}{\partial\alpha_c'}\Delta\alpha_c'\right)^2 + \left(\frac{\partial\eta}{\partial\alpha_c}\Delta\alpha_c\right)^2, \qquad (11)$$

where the rms component errors were taken as

$$(\Delta\alpha,\ \Delta\alpha',\ \Delta\alpha_f',\ \Delta\alpha_c,\ \Delta\alpha_c')$$
$$= (0.35,\ 2*\Delta\alpha,\ 0.5,\ 0.15,\ 2*\Delta\alpha_c).$$

The coherence of the α and α' errors seems reasonable given that their derivation from measured τ_a spectra is not independent and given the considerable empirical evidence from the processing of various data sets (in terms of the coherence of residuals about a mean). It must be noted, however, that the constant of proportionality between α' and α residuals is quite variable and has been observed to vary from 0 to 3. In addition, the correlation coefficient is not always significant (in particular at small τ_a). It is therefore clear that the error computations of Fig. 2 are fairly approximate.

The curves in Fig. 2 do indicate that α must be greater than approximately 1.0 to achieve minimally acceptable errors ($\Delta\alpha_f \sim 0.5$ or less in a measurable range of approximately 1.0–2.5). The total errors are typically dominated by the error in α', which, in spite of polynomial smoothing, is quite sensitive to any high-frequency structure in τ_a spectra (both $\Delta\alpha$ and $\Delta\alpha'$ are approximately proportional to $\Delta\tau_a/\tau_a$).[2] We note that the error in α_f that is due to the component uncertainty in α_f' was ~0.2 or smaller for the

range of cases defined in the discussions associated with Eq. (7).

In practice (because we can estimate $\Delta\alpha_f$ and $\Delta\eta$ for an individual measurement) we apply an error-dependent weighting scheme to the individual members of a measured set of τ_a spectra, and in doing so we can achieve standard deviations that are similar to the errors illustrated in Fig. 2. In any case, whether one employs our simple algorithm for extracting α_f or a more sophisticated particle size inversion scheme to interpret τ_a spectra, the key to the level of confidence in the retrieved results is α'; if the error associated with this parameter is too large, then significant higher-order spectral variation is partially or even totally obscured and the spectral information content is not much better than the classical (constant α) case.

3. Validation by Simulations

Figure 3 shows α_f and η computations applied to optical depths computed for typical coarse-mode statistics and a modeled accumulation mode whose effective radius gradually increases from approximately 0.1 to 0.2 μm as a function of aerosol optical depth (from Ref. 2 by use of a model that is similar to Ref. 12). The mean and standard deviation statistics of τ_c shown in Table 2 were employed to generate three curves corresponding to minimum, mean, and upper-limit coarse-mode variations whereas τ_f was allowed to increase progressively.

We obtained the solid red curves and the accompanying dashed red curves of Figs. 3(a) and 3(b) using Eq. (9) and (6) at a wavelength of 500 nm. These curves correspond to the three extremes of τ_c [the dashed curves are barely perceptible in Fig. 3(a)]. The blue curves in Figs. 3(a) and 3(b) correspond to the true (input) values of α_f and η, respectively, for the three extremes of τ_c. The differences between the true values and the estimated values of α_f and η are due to the errors in the approximation of α_f' given by Eq. (7) and small deviations from the exact values of α_c and α_c'. The lower set of solid and dashed curves in Fig. 3(a) correspond to the value of α at 500 nm and are included to show the relative importance of the α_f transformation and how the transformation eliminates Ångström exponent differences that are due to (abundance-induced) variations in η.

It is clear that the transformation from α to α_f in Fig. 3(a) significantly reduces the influence of abundance or particle number and enables one to obtain a parameter that is largely dependent on average particle size of the fine mode. Also, one can observe [Fig. 3(b)] that realistic estimates of η are obtained from the estimates of α_f [Eq. (6)].

It is critical to emphasize that the processing required to extract these parameters, not unlike the smoothing that occurs for the classical multiband Ångström exponent, must be carried out on optical depth spectra that have been regressed by a second- or third-order polynomial. This polynomial fitting procedure is necessary to (i) obtain a nonzero value for α' and (ii) reduce noise effects in α and α'. The
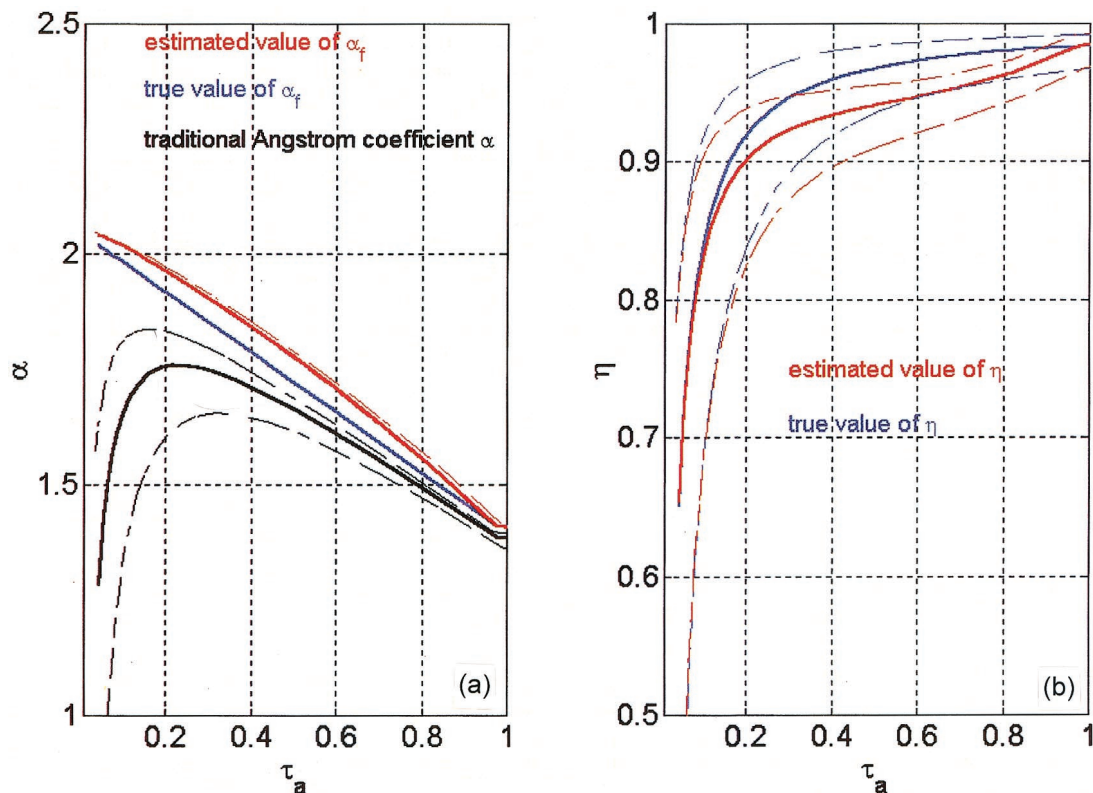
Fig. 3. Simulations of (a) α and α_f versus τ_a and (b) η versus τ_a at the standard wavelength of 500 nm. The red curves represent estimates of α_f and η from the fine-mode extraction algorithm [Eqs. (9) and (6), respectively] and the blue curves are the true simulation values of these parameters. The lower curves in (a) show the corresponding variations in α for the means and standard deviations of τ_c given in Table 2.

polynomial fits also permit a convenient and standard definition of a nominal monochromatic wavelength such as the 500-nm wavelength used throughout this paper. It must also be noted that, for N_λ wavelength bands, the order of the polynomial should probably not exceed $N_\lambda - 2$ where $N_\lambda \geq 4$. For example, a third-order fit to a four-wavelength optical depth spectra is typically more sensitive to spectral variations because such a fit amounts to a zero residual polynomial through all four error-prone points rather than a smoothing regression.

4. Application to Measured Data

In this section we present sample computations of α_f and η using data acquired by CIMEL sunphotometers of the Aerosol Robotic Network (AERO-NET).[14,15] The CIMEL instruments (specifically reference units 37 and 101, which were calibrated at Mauna Loa Observatory) collect aerosol optical depth data across seven channels (340, 380, 440, 500, 670, 870, and 1020 nm) and sky radiance measurements

in the solar almucantar across four spectral channels (440, 670, 870, and 1020 nm). These latter measurements are used, along with associated optical depth measurements at the same four channels, to perform inversions for particle size distribution and refractive index.[16] It should be noted that the seven-channel optical depth measurements and the four-channel sky radiance and optical depth (inversion) measurements define two physically different data sets. Also, for reasons that are mostly related to the difficulties in the calibration of the 340-nm channel, we excluded this channel from the former data set. The resulting six-channel optical depth spectra were fitted to a third-order polynomial [$\ln \tau_a = P^{(3)} (\ln \lambda)$] from which α and α' were computed at the standard wavelength of 500 nm.

A. Temporal Estimates of α_f

Figure 4 shows the temporal variation of the key optical parameters associated with the fine-mode extraction algorithm for cloud-screened optical depth

Table 2. Course-Mode Optical Depth Extrema Used in the Simulation (Interpolated to 500 nm)[a]

	$\langle \log_{10}(\tau_x) \rangle + \mathrm{SD}^b$	$10^{\log 10(\tau_x) - \mathrm{SD}}$	$10^{\log 10(\tau_x)}$	$10^{\log 10(\tau_x) + \mathrm{SD}}$
τ_c	-1.80 ± 0.30	0.008	0.016	0.032

[a]These statistics were calculated from 930 particle size distribution inversions.[2]
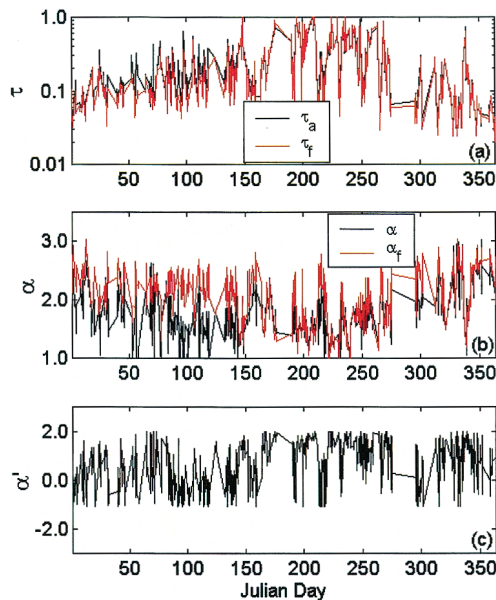[b]SD, standard deviation.

Fig. 4. Temporal variation of key parameters associated with α_f and η estimation as a function of Julian Day for optical depth spectra acquired during 1998 at the NASA Goddard Space Flight Center AERONET site in Greenbelt, Maryland. The data were filtered such that all points outside of the range $-1.1 < \alpha' < 2$ are excluded (4429 data points remained from the original 5050 spectra). $\lambda = 500$ nm.
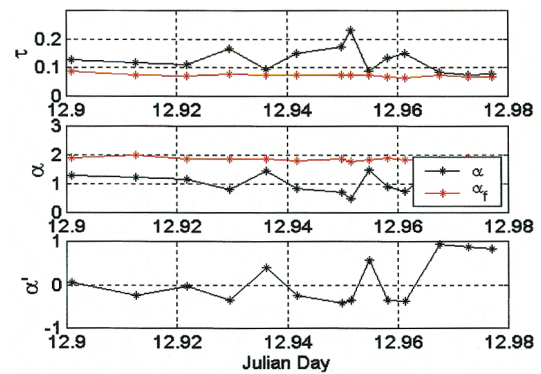

Fig. 5. Thin-cloud-contaminated optical depth as a function of time for CIMEL data acquired at Egbert, Ontario, and the variance reduction brought about by the transformation of Eqs. (9) and (6). The figure arrangement and color schemes are the same as in Fig. 4 ($12.5 \Rightarrow$ Greenwich Mean Time noon on 12 August 1998). These data were not cloud screened and no α' filter was applied. $\lambda = 500$ nm.

data acquired at the Goddard Space Flight Center in Greenbelt, Maryland, during the whole of 1998.[2,17] In these graphs the input and output parameters to the α_f and η extraction algorithms appear as black and red curves, respectively. The temporal variation of τ_a in Fig. 4(a) shows typical seasonal behavior characterized by greater turbidities in the spring to autumn period. The values of τ_f computed from Eq. (6) are in general of the order of or less than τ_a (i.e., $\alpha - \alpha_c < \alpha_f - \alpha_c$). Figure 4(b) shows the variation in α and the estimated value of α_f derived from Eq. (9). The two parameters are similar in magnitude during the summer season when the optical depth is larger or when one would expect that the fine-mode particle size distribution is dominant. During the rest of the year, when aerosol optical depths are smaller and less dominated by the fine-mode size distribution, α_f is typically greater than α. It is worth noting that the size evolution of the accumulation mode as a function of optical depth alluded to in Section 3 is effectively magnified by the increase in α_f (associated with a real decrease in the effective radius of the accumulation mode) during the winter and spring months.

In Fig. 4(c), α' is typically less than the nominal value of α_f' (which is in the neighborhood of 1.2) from approximately day 1 to day 150 (and less evidently from approximately day 275 to day 365) so that α is generally less than α_f. During the summer months α' is of the order of the nominal value of α_f' (around 1.5 or slightly larger), and the curves of α_f and τ_f are roughly superimposed on the α and τ_a curves, respectively. Values of α_f that are slightly less than α also

occur during this season. Although it is true that α' cannot be greater than the true value of α_f' [see Eq. (3)], it can certainly be greater than the nominal value of α_f' given by Eq. (7).

The data of Fig. 4, in addition to being effectively filtered by a third-order spectral polynomial, were further constrained by the condition $-1.1 < \alpha' < 2$ at 500 nm. This type of data screening reduced the variance in the computed value of α_f without significantly changing average trends. The upper-limit constraint on α' corresponds to the condition that $\alpha' < \alpha_f'$ for $\eta < 1$ whereas the lower limit was computed from the extreme values of α_f and α_f' that were employed to determine Eq. (7) (from Ref. 2 by use of α'_{min}). Values of α' outside these bounds represent spectral artifacts that could include residual interband calibration errors at small optical depths, spectrally dependent nonlinearities at low signal levels, and effects of small amounts of gaseous absorption not accounted for in the computed aerosol optical depths (such as NO_2 at 380–500 nm and H_2O at 1020 nm).

B. Application to Thin-Cloud Data

Figure 5 illustrates the physical consistency of the α_f extraction algorithm for a sampling of (thin) cloud-contaminated optical depth data acquired on 12 August 1998 at Egbert, Ontario, Canada. Our criteria for labeling a given set of points as thin cloud were a combination of intermediate to large optical depth accompanied by relatively small values of α and a temporal behavior that typically showed an inverse variation between the two parameters (behavior that is evident in Fig. 5). Thin cloud effectively represents a coarse mode that satisfies the conditions set forth when we derived Eq. (5) and thus is an opportune means of testing the concept that extensive variations of abundance (optical depth) are the cause of variations in α. A verification of the robustness of the algorithm is clearly whether the large changes in
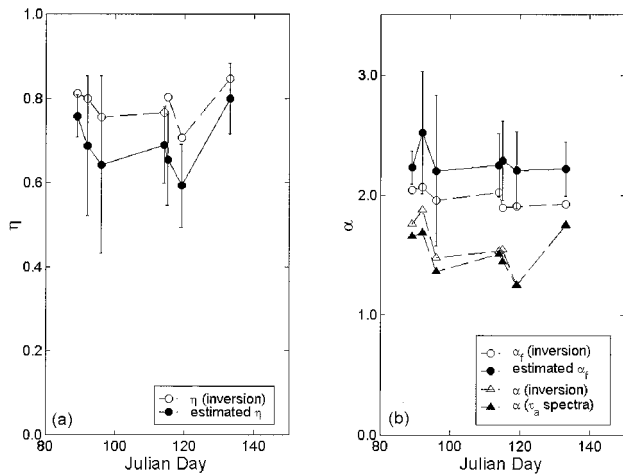
Fig. 6. (a) Comparison of η estimates by use of Eq. (6) on a sample temporal profile of six-channel data (filled circles) and computations of η for size distribution inversions from nearly synchronous almucantar and (four-channel) optical depth data (open circles); (b) comparison of α_f by use of Eq. (9) with inversion estimates of α_f. $\lambda = 500$ nm along with the original (measured) and inversion values of α. The label inversion refers to the process of extracting a size distribution and refractive index,[13] partitioning the size distribution at 0.6 μm, and then returning to the optical domain to calculate α_f and η.

Fig. 7. Actual size distributions used to compute the inversion profiles of Fig. 6. The division into fine and coarse modes was set at a 0.6-μm radius. This division permitted the computation of fine- and coarse-mode optical depths and thus validation data for the fine-mode extraction algorithms.

α that can be seen in the middle graph of Fig. 5 would be effectively filtered out by the α_f transformation. One can observe that this is largely the case and that the strong temporal correlation between α and α' is the driving mechanism for this filtering. This type of variance reduction in transforming from τ_a and α to τ_f and α_f seems to be a fairly typical occurrence for conditions determined to represent thin cloud.

C. Comparisons with Size Distribution Inversions

Figure 6 is a comparison of η and α_f estimates by use of Eqs. (9) and (6) on a sample profile of six-channel data with computations of η and α_f for size distribution inversions from nearly synchronous almucantar and (four-channel) optical depth data.[16] In the latter case we extracted the fine-mode size distribution from the inversions by assuming a partitioning of the volume size distribution across a radius of 0.6 μm. We then computed true fine-mode optical parameters (τ_f and α_f) by using the Mie kernels employed in the inversion to return to the optical domain.

The comparison between the estimated values of η and α_f and the values derived from particle size distribution inversions for the seven samples of Fig. 6 yield reasonable results with rms differences of approximately 0.10 in η and 0.31 in α_f (note, for example, that the differences in the α_f estimates are less than the change from the α curve to the α_f curve). We estimated the error bars shown on the η and α_f estimates (average magnitudes of 0.11 and 0.34, respectively) based on Eqs. (10) and (11) (note that the relatively small errors associated with α_f', α_c, and α_c' were ignored). The fundamental $\Delta\tau_a$ errors were taken as a quadrature sum of the polynomial fitting
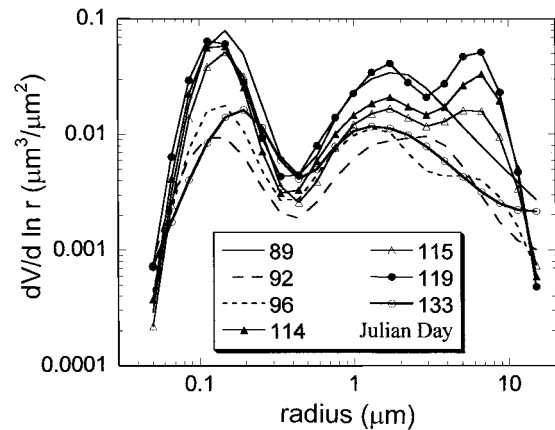
residuals and the estimated instrumental error (~0.01 in optical depth) at 500 nm. The larger errors for the second and third points of the temporal series are associated with relatively small aerosol optical depth (τ_a ranges from approximately 0.08 to 0.30). The error bars obtained for the inversion-based estimates of η and α_f (not shown in Fig. 6) are estimated to be of similar magnitude.

The actual inversion size distributions for the temporal sample of Fig. 6 are shown in Fig. 7. It is important to observe that the coarse-mode size distribution can be quite variable in form and even appears as a bimodal distribution in some cases. However, the only practical coarse-mode constraint required in the application of Eqs. (9) and (6) is that α_c and α_c' be small (approximately invariant to be specific). In point of fact the 930 inversions that contributed to the statistics of Table 2 yielded a mean value of $\alpha_c = -0.16 \pm 0.03$ at 500 nm (estimates of α_c' were small as expected from Mie theory, but were too statistically variable to warrant any action other than the convenient assumption of zero).

It is noted that a final small adjustment downward of the α and α_f values computed from the inversion had to be performed because these estimates could return small systematic differences in α (and by inference α_f) relative to the original four-channel measurements. The particle size distribution inversions are constrained to produce small errors in almucantar radiance and τ_a; small but systematic spectral errors in α can survive this process, and accordingly it was necessary to adjust the inversion results such that this artifact was eliminated from the four-channel data.

5. Conclusions

A simple procedure is presented for the extraction of an Ångström exponent and the optical fraction of the fine-mode portion of the particle size distribution without a prohibitive increase in the complexity of

optical processing (relative to the level of processing required to extract a value of the classical Ångström parameter). In the case of the Ångström exponent this procedure permits a decoupling of intensive fine-mode information (size and refractive index) from the extensive variations associated with the influence of relative modal abundance on the traditional Ångström exponent.

Computations over a year's worth of six-channel aerosol optical depth data show that the predictions of the extraction procedure are physically coherent with values of α_f, are systematically larger than α during the winter months, and are of the same order of magnitude during the summer months. A good test of the physical coherency of the α_f and η estimation algorithm was to show that stable values of α_f and τ_f could be extracted from variable α and α' data that were thought to be associated with thin cloud. Finally, values of α_f estimated from six-channel data were found to be comparable to a sampling of values computed from particle size distribution inversions derived from sky radiance and optical depth data.

References

1. A. Ångström, "On the atmospheric transmission of sun radiation and on dust in the air," Geogr. Ann. Dtsch. **12,** 156–166 (1929).
2. N. T. O'Neill, T. F. Eck, B. N. Holben, A. Smirnov, and O. Dubovik, "Bi-modal size distribution influences on the variation of Angstrom derivatives in spectral and optical depth space," J. Geophys. Res. (to be published).
3. J. S. Reid, T. F. Eck, S. A. Christopher, P. V. Hobbs, and B. N. Holben, "Use of the Angstrom exponent to estimate the variability of optical and physical properties of aging smoke particles in Brazil," J. Geophys. Res. **104,** 27473–27489 (1999).
4. T. F. Eck, B. N. Holben, J. S. Reid, O. Dubovik, A. Smirnov, and N. T. O'Neill, "The wavelength dependence of the optical depth of biomass burning, urban, and desert dust aerosols," J. Geophys. Res. **104,** 31333–31350 (1999).
5. K. S. Shifrin, "Simple relationships for the Ångström parameter of disperse systems," Appl. Opt. **34,** 4480–4485 (1995).
6. N. T. O'Neill and A. Royer, "Extraction of bimodal aerosol-size distribution radii from spectral and angular slope (Angstrom) coefficients," Appl. Opt. **32,** 1642–1645 (1993).
7. A. Ångström, "The parameters of atmospheric turbidity," Tellus **16,** 64–75 (1964).
8. World Meteorological Organization, "Report of the experts meeting on aerosols and their climatic effects," World Climate Research Program, Rep. WCP-55 (World Meteorological Organization, Geneva, Switzerland, 1983).
9. E. M. Patterson and D. A. Gillette, "Commonalities in measured size distribution for aerosols having a soil-derived component," J. Geophys. Res. **82,** 2074–2082 (1977).
10. E. P. Shettle and R. W. Fenn, "Models for the aerosol of the lower atmosphere and the effects of humidity variations on their optical properties," Environmental Research Paper 767, AFGL-TR-79-0214 (U.S. Air Force Geophysics Laboratory, Hanscom Air Force Base, Mass., 1979).
11. J. E. Hansen and L. D. Travis, "Light scattering in planetary atmospheres," Space Sci. Rev. **16,** 527–610 (1974).
12. L. Remer, Y. J. Kaufman, and B. N. Holben, "Interannual variation of ambient aerosol characteristics on the East Coast of the United States," J. Geophys. Res. D2 **104,** 2223–2231 (1999).
13. H. C. van de Hulst, *Light Scattering by Small Particles* (Wiley, New York, 1957).
14. B. N. Holben, T. F. Eck, I. Slutsker, D. Tanre, J. P. Buis, A. Setzer, E. Vermote, J. A. Reagan, Y. Kaufman, T. Nakajima, F. Lavenu, I. Jankowiak, and A. Smirnov, "AERONET—a federated instrument network and data archive for aerosol characterization," Remote Sens. Environ. **66,** 1–16 (1998).
15. A. Smirnov, B. N. Holben, T. F. Eck, O. Dubovik, and I. Slutsker, "Cloud screening and quality control algorithms for the AERONET data base," Remote Sens. Environ. **73,** 337–349 (2000).
16. O. Dubovik and M. D. King, "A flexible inversion algorithm for retrieval of aerosol optical properties from sun and sky radiance measurements," J. Geophys. Res. **105,** 20673–20696 (2000).
17. B. N. Holben, D. Tanre, A. Smirnov, T. F. Eck, I. Slutsker, N. Abuhassan, W. W. Newcomb, J. Schafer, B. Chatenet, F. Lavenue, Y. J. Kaufman, J. Vande Castle, A. Setzer, B. Markham, D. Clark, R. Frouin, R. Halthore, A. Karnieli, N. T. O'Neill, C. Pietras, R. T. Pinker, K. Voss, and G. Zibordi, "An emerging ground-based aerosol climatology: aerosol optical depth from AERONET," J. Geophys. Res. (to be published).